SCIENCE CHINA
Earth Sciences

Complete three-dimensional coseismic displacements due to the 2021 Maduo earthquake in Qinghai Province, China from Sentinel-1 and ALOS-2 SAR images

Jihong Liu[1], Jun Hu[2], Zhiwei Li[3], Zhangfeng Ma[4], Lixin Wu[5], Weiping Jiang[6], Guangcai Feng[7] and Jun Zhu[8]

Citation: SCIENCE CHINA Earth Sciences (2021); doi: 10.1007/s11430-021-9868-9

View online: https://engine.scichina.com/doi/10.1007/s11430-021-9868-9

Published by the Science China Press

Complete three-dimensional coseismic displacements due to the 2021 Maduo earthquake in Qinghai Province, China from Sentinel-1 and ALOS-2 SAR images

Jihong LIU[1], Jun HU[1*], Zhiwei LI[1], Zhangfeng MA[2], Lixin WU[1], Weiping JIANG[3], Guangcai FENG[1], Jianjun ZHU[1]

[1] School of Geosciences and Info-Physics, Central South University, Changsha 410083, Hunan, China

[2] School of Earth Sciences and Engineering, Hohai University, Nanjing 211100, Jiangsu, China

[3] GNSS Research Center, Wuhan University, Wuhan 430079, China

*** Corresponding author** (email: csuhujun@csu.edu.cn)

Abstract On 22nd May 2021 (local time), an earthquake of Ms7.4 struck Maduo county in Qinghai Province, China. This was the largest earthquake in China since the 2008 Wenchuan earthquake. In this study, ascending/descending Sentinel-1 and advanced land observation satellite-2 (ALOS-2) synthetic aperture radar (SAR) images were used to derive the three-dimensional (3-D) coseismic displacements of this earthquake. We used the differential interferometric SAR (InSAR, DInSAR), pixel offset-tracking (POT), multiple aperture InSAR (MAI), and burst overlap interferometry (BOI) methods to derive the displacement observations along the line-of-sight (LOS) and azimuth directions. To accurately mitigate the effect of ionospheric delay on the ALOS-2 DInSAR observations, a polynomial fitting method was proposed to optimize range-spectrum-split-derived ionospheric phases. In addition, the 3-D displacement field was obtained by a strain model and variance component estimation (SM-VCE) method based on the high-quality SAR displacement observations. Results indicated that a left-lateral fault slip with the largest horizontal displacement of up to 2.4 m dominated this earthquake, and the small-magnitude vertical displacement with an alternating uplift/subsidence pattern along the fault trace was more concentrated in the near-fault regions. Comparison with the global navigation satellite system data indicated that the SM-VCE method can significantly improve the accuracy of the displacements compared to the classical weighted least squares method, and the incorporation of the BOI displacements can substantially benefit the accuracy of north–south displacement. In addition to the displacements, three coseismic strain invariants calculated based on the strain model parameters were also investigated. It was found that the eastern and western parts of the faults suffered more significant strains compared with the epicenter region.

Keywords: The 2021 Maduo earthquake, 3-D displacements, SM-VCE, SAR, Coseismic strain field

1. Introduction

At 02:04:13 on 22ed May 2021 (local time), an earthquake of Ms7.4 struck Maduo County in Qinghai Province, China (Li et al., 2021b). This was the largest earthquake in China since the 2008 Wenchuan earthquake. The epicenter was located about 38 km southeast of Maduo county at a depth of about 17 km. Field investigations show that this earthquake caused ground surface displacements of up to several meters, and induced many cracks, geysers, and seismic bulges (Li et al., 2021c; Pan et al., 2021). The earthquake occurred on a known left-lateral strike-slip fault (i.e., Jiangcuo fault in Figure 1) in the northeastern part of the Bayankala block, which is about 70 km south of the Tuosuo Lake segment of the East Kunlun fault zone. If the Jiangcuo fault extends westward, it can be connected with the Kunlun Mountain Pass fault, on which an earthquake of M8.1 occurred in 2001 (Pan et al., 2021). The tectonic background in this region is very complicated. This complexity mainly relates to the

northward push of the Indian block, the uplift of the Qinghai-Tibet Plateau block, and the eastward extrusion of the Bayankala sub-block. The Bayankala block is bounded by the Longmenshan fault zone, the Yushu-Ganzi-Xianshuihe fault zone, the Altun Tagh fault zone, and the Kunlun fault zone in the east, south, west, and north directions, respectively (Pan et al., 2021; Zhan et al., 2021). In recent years, several strong earthquakes have occurred around the periphery of the Bayankala block (e.g., the 2001 M8.1 Kunlun earthquake, the 2008 M8.0 Wenchuan earthquake, the 2010 M7.1 Yushu earthquake, the 2013 M7.0 Lushan earthquake, and the 2017 M7.0 Jiuzhaigou earthquake) (Wang et al., 2021; Zhu et al., 2021), and the occurrence of the 2021 Maduo earthquake seems to spatially fill the Ms>7.0 seismic gap around the Bayankala block (Wang et al., 2021) (see Figure 1c).

Ground surface displacement is one of the most intuitive manifestations of earthquakes, and provides important perspectives for conducting disaster evaluation, constraining the fault slip model, and understanding the triggering mechanism (Hu et al., 2021). Synthetic aperture radar (SAR) images that are actively acquired from satellites can be used to effectively obtain the ground surface displacement field with high accuracy and high spatial resolution (Bürgmann et al., 2000; Li and Bürgmann 2021). For a pair of SAR images, based on the phase information, the differential interferometric SAR (InSAR, DInSAR) (Gabriel et al., 1989) and the multiple aperture InSAR (MAI) (Bechor and Zebker 2006; Jung et al., 2009) methods can be used to obtain the ground surface displacement along the satellite line-of-sight (LOS) and the azimuth (AZI) directions, respectively. In addition, based on the amplitude information of SAR images, the pixel offset-tracking (POT) (Michel et al., 1999) method can be used to simultaneously obtain the displacement along the LOS and AZI directions. In particular, benefitting from the terrain observation by progressive scans (TOPS) imaging mode of Sentinel-1 SAR data (Torres et al., 2012), a burst overlap interferometry (BOI) method (Grandin et al., 2016), relying on the phase information, was developed to obtain the AZI displacement for only the overlap area of two successive bursts. In terms of the imaging geometry of the displacement observations, the DInSAR method can only obtain the LOS displacements, the MAI and BOI methods can only obtain the AZI displacements, and the POT method can obtain both the LOS and AZI displacements. With one or more of these methods, it is feasible to obtain a reliable displacement field that can well constrain the fault movement.

In addition to the ground surface displacements, the surface strain field is another physical quantity that can be used to assess the relative displacement and subsequent changes in particle configuration in each dimension of the Earth body (Cardozo and Allmendinger 2009; Okada 1985). A large number of studies have been conducted on the strain field (e.g., Clarke et al., 1998; Hu et al., 2014; Lin et al., 2010; Mehrabi 2021; Pietrantonio and Riguzzi 2004; Savage and Lisowski 1994; Shen et al., 1996), most of which are based on the global navigation satellite system (GNSS) and the triangulation data. Open software packages have also been released for the calculation of the strain field based on these sparse observations (e.g., Cardozo and Allmendinger 2009; Goudarzi et al., 2015; Teza et al., 2008). Since the displacement field and the strain field reflect different perspectives of the ground deformations, it is feasible to reveal the complete deformation pattern of ground surface by combining these two kinds of field.

In this study, both Sentinel-1 and advanced land observation satellite-2 (ALOS-2) SAR data from ascending and descending orbits (four pairs of SAR images in total) were used to map the complete three-dimensional (3-D) coseismic displacement associated with the 2021 Maduo earthquake. All of the above methods (i.e., DInSAR, MAI, BOI, and POT) were used to obtain displacement observations. Because individual displacement observation only captures one-dimensional (1-D) projection of the 3-D displacements in a particular direction (e.g., LOS or AZI), it is difficult to directly relate them to the real surface movements (Fialko et al., 2005; Funning et al., 2005; He et al., 2019; Jung et al., 2011; Wright et al., 2004). By combining these displacement

observations, we calculated the 3-D displacements of the 2021 Maduo earthquake with a newly proposed SM-VCE method (Liu et al., 2018) (a method for measuring 3-D surface displacements with InSAR based on a strain model (SM) and variance component estimation (VCE)). Previous studies (Hu et al., 2021; Liu et al., 2018; Liu et al., 2019) have demonstrated the superiority of the SM-VCE method for estimating more accurate 3-D displacements compared with the classical weighted least squares method. Furthermore, we calculated three strain invariants based on the strain model parameters and analyzed the spatial pattern of the coseismic strain field in combination with the 3-D displacement field. In particular, the displacement and strain result in this paper can be freely accessed through https://dx.doi.org/10.5281/zenodo.5009820.

2. Materials and methods

2.1. The processed SAR data

As the new generation of European Space Agency's (ESA) C-band SAR mission, Sentinel-1, comprised of two satellites that were launched on 3rd April 2014 and 16th April 2016, usually acquires regular TOPS-mode SAR data and freely provides the SAR data to the public. Therefore, it is generally the first choice for SAR data when investigating the displacement with respect to earthquakes, landslides, etc. (e.g., Funning and Garcia 2019; Intrieri et al., 2018; Liu et al., 2021a). On 24th May 2014, the Japan Aerospace Exploration Agency (JAXA) launched the ALOS-2 mission, which can acquire the L-band SAR data with both strip-map and ScanSAR modes. Due to the longer wavelength of the L-band compared with the C-band SAR data, the ALOS-2 SAR data is more capable of suppressing decorrelation noise. Therefore, ALOS-2 data is also commonly used to measure the coseismic displacement (e.g., Gan et al., 2018; Xu et al., 2018). For the 2021 Maduo earthquake, both Sentinel-1 and ALOS-2 SAR data from ascending and descending orbits are available several days after an earthquake. The basic information of the SAR data used herein is shown in Table 1, and the footprints of these SAR data can be found in Figure 1. It should be noted that both Sentinel-1 and ALOS-2 SAR data were acquired at least 3 days after the earthquake event, thus it is inevitable to include the postseismic displacements in the derived SAR displacement fields. The mistake of including the postseismic displacement in the coseismic displacement may lead to the a misestimation of slip distribution and seismic moment. Nevertheless, compared to the coseismic displacement, the postseismic displacement is probably negligible as historical postseismic displacements recorded in other large strike-slip earthquakes (Ms>7.0) did not reach a relatively high level (e.g., Fialko 2004; Fialko et al., 2005; Jacobs et al., 2002). Therefore, it is reasonable to believe that the SAR displacements obtained in this paper are dominated by the coseismic displacement.

Table 1. Basic information of the SAR data used herein.

Sensor	Orbit direction	Master and slave date	Spatial perpendicular baseline (m)	Wavelength (cm)	Incident angle (deg.)	Azimuth angle (deg.)	Pixel resolution (m)(range × azimuth)	Imaging mode
Sentinel-1	Ascending	2021-05-20 2021-05-26	54	5.6	39.5	-13.0	2.33×13.98	TOPS
Sentinel-1	Descending	2021-05-20 2021-05-26	109	5.6	39.6	-167.0	2.33×13.97	TOPS
ALOS-2	Ascending	2020-05-25 2021-05-24	-190	23.6	36.2	-12.7	4.29×3.78	Strip-map
ALOS-2	Descending	2020-12-04 2021-06-04	197	23.6	39.0	-170.0	8.58×2.64	ScanSAR

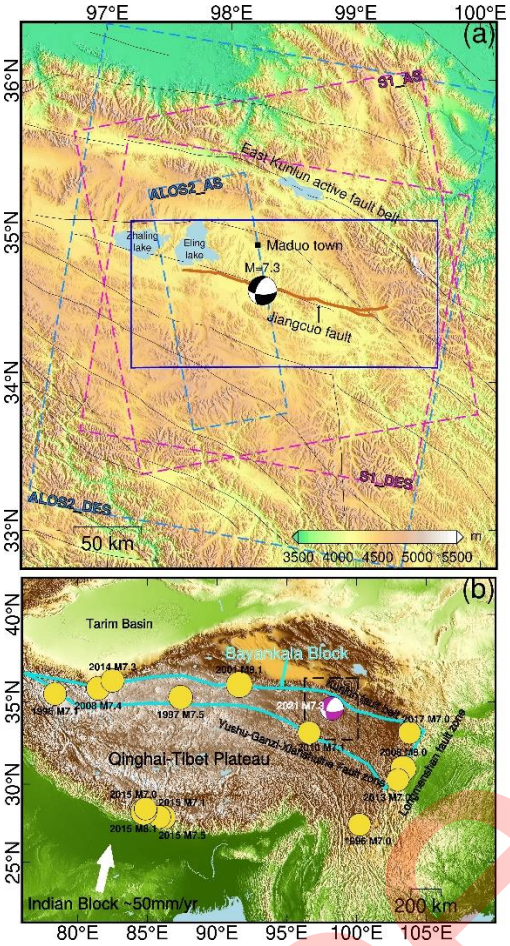

Figure 1 (a) Color-shaded relief map. The dashed rectangles outline the footprint of SAR data, and the blue rectangle outlines the study area focused on (e.g., the range in Figure 2 and Figure 4) in this paper. The black lines show the location of known faults, where the east Kunlun active fault belt and the Jiangcuo fault are labeled. The brown lines are the ruptured fault traces of the 2021 Maduo earthquake, which are manually sketched based on the Sentinel-1 POT observations. The beach ball represents the focal mechanism and epicenter location from the USGS. The location of the Maduo town is represented by the black square. (b) The distribution of M>7.0 earthquakes around the Qinghai-Tibet Plateau. The dashed rectangle outlines the range of (a).

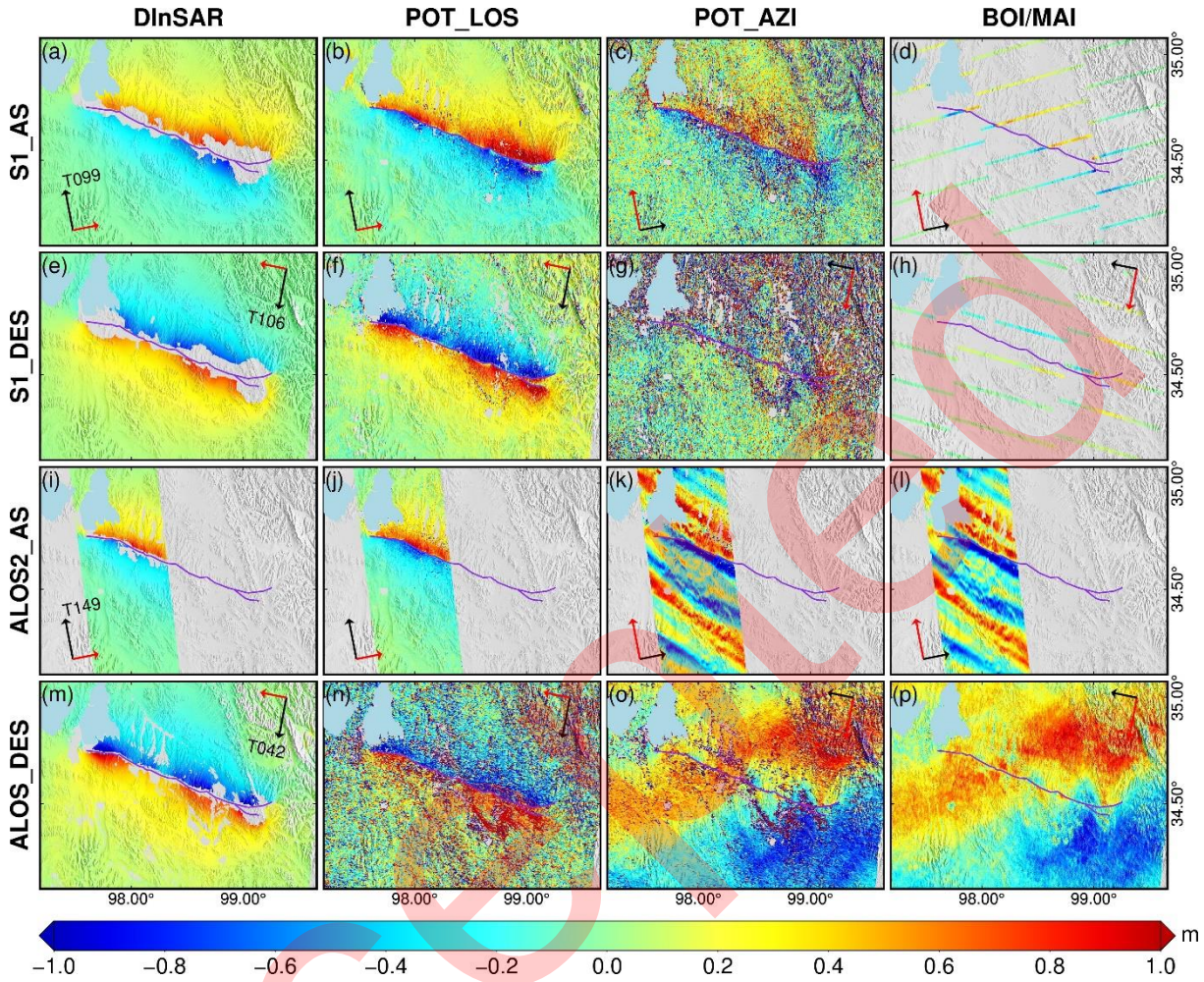

Figure 2 Displacement observations along the LOS and AZI directions from ascending/descending Sentinel-1/ALOS-2 SAR data based on the DInSAR, POT, MAI, and BOI methods. Longer and shorter arrows represent the AZI and LOS directions, respectively, the red arrow corresponds to the observing direction of each observation, and the orbit track numbers are labelled in the DInSAR maps. The purple lines show the location of ruptured fault traces. The displacements within the range of the whole SAR image are shown in Figure S1.

Here, the DInSAR, MAI, POT, and BOI methods were employed to process the ascending/descending Sentinel-1/ALOS-2 SAR images, and the detailed processing procedure can be found in Appendix A(http://link.springer.com). For a pair of SAR images, the DInSAR method is usually the first choice for measuring the ground surface displacement (Ma et al., 2021), which is the projection of 3-D displacements along the LOS direction. Since the current SAR data are mostly acquired by the near-polar orbit satellites in the right-looking imaging mode, the DInSAR-derived displacements are only available in two distinct geometries (i.e., ascending and descending LOS directions), and cannot well constrain the 3-D displacements, particularly the north-south displacement component. The MAI, POT, and BOI methods can all derive the displacement observation along the satellite AZI direction. Because the AZI direction is almost parallel to the N-S direction, the AZI displacement observations derived by these methods can well compensate for the missing N-S displacement information in the LOS displacement observations. Although the BOI-obtained AZI observations are only available in the burst overlaps of Sentinel-1 SAR data, they provide the key information for constraining the 3-D displacements when other AZI observations are not available (Grandin et al., 2016).

Figure 2 presents the obtained SAR displacement observations. For the sake of simplicity, the combination of

several abbreviations linked by underline characters is used to represent the corresponding SAR displacement observation. For example, ALOS2_AS_DInSAR represents the DInSAR observation of ascending (AS) ALOS-2 data, S1_DES_POT_AZI represents the POT observation of descending (DES) Sentine1-1 (S1) data along the AZI direction, and S1_DInSAR represents the DInSAR observations of S1 data from both ascending and descending orbits. As shown in Figure 2, the displacement observations with similar geometry are consistent with each other (e.g., S1_DES_DInSAR (Figure 2e), ALOS2_DES_DInSAR (Figure 2m), and S1_DES_POT_LOS (Figure 2f)). Due to the longer wavelength of the ALOS-2 data compared to the Sentinel-1 data, the measurable displacement gradient of DInSAR method of the ALOS-2 data is higher than that of the Sentinel-1 data; therefore, the ALOS2_DInSAR observations (Figure 2i and Figure 2m) can achieve a more complete displacement field in the near-fault regions compared to the S1_DInSAR observations (Figure 2a and Figure 2e). However, the ALOS-2 data suffer serious ionospheric disturbances (Figure 2k, Figure 2l, Figure 2o and Figure 2p), and their effect on the DInSAR observations cannot be ignored. Although a range spectrum split (RSS) method can be used to estimate the ionospheric phase, this is highly sensitive to decorrelation noise. In this study, a polynomial fitting (PolyFit) method was proposed to optimize the RSS-derived ionospheric phase, particularly in the low-coherence near-fault regions. Details of the proposed method can be found in Section 2.2. Compared with the LOS displacements (e.g., Figure 3f), the effect of ionospheric delay on AZI displacements is more serious and complex (Figure 2k, 2l, 2o, and 2p). As can be seen, the ionospheric phases in the AZI displacements observations are banded, and completely aliasing with the displacement signals, which makes it difficult to separate the ionospheric phases from the displacements signals. Through qualitative comparison, the accuracy of the POT observations is lower than that of the DInSAR and BOI observations, and is proportional to the pixel resolution. One prominent advantage of the POT method is that it can be used to obtain a complete displacement field even in the DInSAR decorrelated regions (e.g., Fialko et al., 2001; Shi et al., 2017; Wang et al., 2018).

2.2 The polynomial fitting method for correcting the ionospheric phase delay

The proposed PolyFit method obtains the ionospheric phase based on the low-accuracy RSS-derived ionospheric phases (Figure 3b), in which those regions with strong ionospheric fluctuations are first masked (Figure 3c). As can be seen from Figure 3a and Figure 3f, the ionospheric phases in the SAR LOS displacement observations are generally low-pass signals in small regions; therefore, can be fitted by polynomials. In this case, the ionospheric phases can be optimized and recovered in the whole region (Figure 3d) based on the RSS ionospheric phases in the unmasked regions.

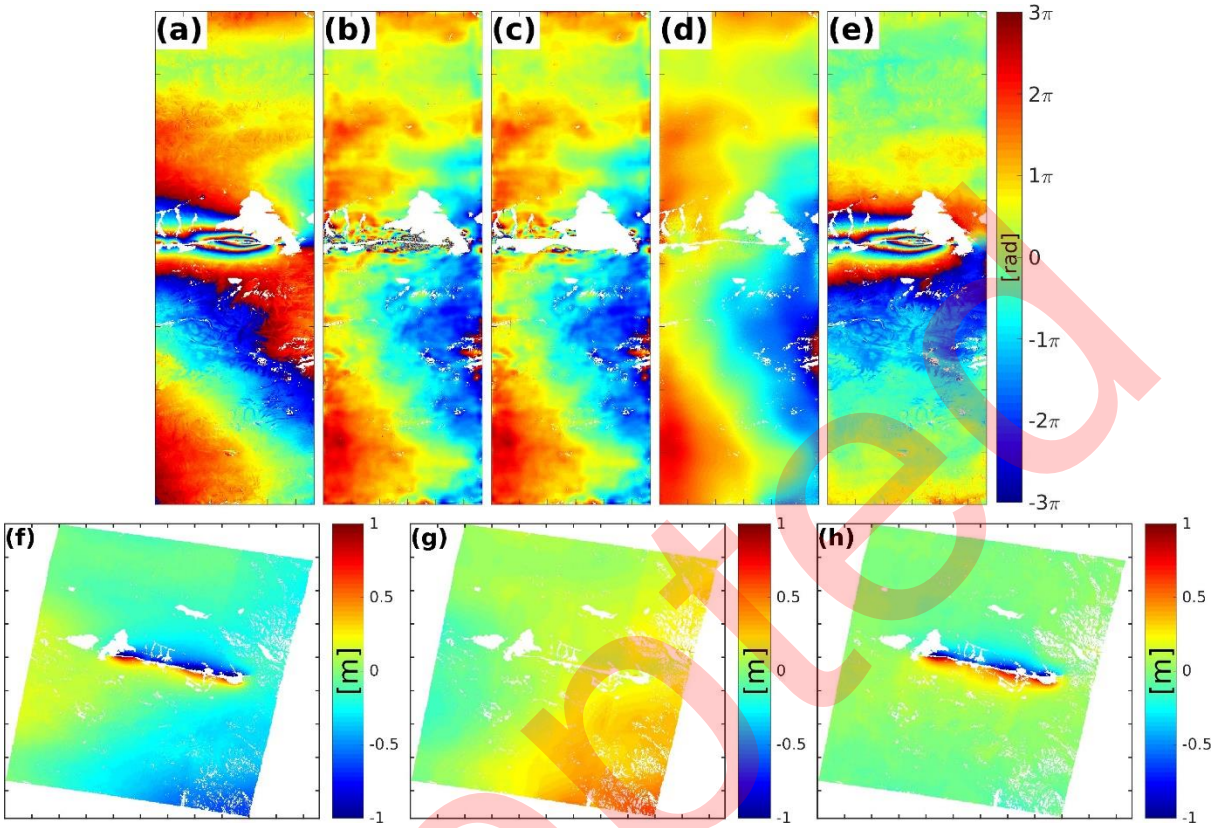

Figure 3. (a)-(e) show an example procedure of the proposed PolyFit method for the ionospheric delay correction with respect to the third beam of the descending ALOS-2 data. (a) The original interferogram. (b) The original RSS-derived ionospheric phase. (c) The original RSS-derived ionospheric phase with masking of the strong fluctuation regions. (d) The ionospheric phase derived by the proposed PolyFit method. (e) The interferogram after the ionospheric phase correction. (a)-(e) share the same colormap and are rewrapped here to improve the display. (f)-(h) show the ALOS-2 DInSAR displacements maps before and after the ionospheric delay correction. (f) The original descending ALOS-2 DInSAR displacements. (g) The ionospheric delay optimized by the proposed PolyFit method based on the RSS result. (h) The DInSAR displacements after ionospheric delay correction.

We assume there are K valid pixels (x_k, y_k), $k = 1, 2, \ldots, K$ around a target pixel (x_0, y_0) and the original RSS-derived ionospheric phases at those K pixels are $\boldsymbol{\varphi}_{\text{rss}} = \left[\varphi_{\text{rss},1}, \varphi_{\text{rss},2}, \ldots, \varphi_{\text{rss},K}\right]^T$. Let

$$\boldsymbol{B}_{\text{rss}} = \begin{bmatrix} 1 & x_1 & y_1 \\ 1 & x_2 & y_2 \\ \vdots & \vdots & \vdots \\ 1 & x_K & y_K \end{bmatrix} \tag{1}$$

The fitting polynomial parameters $\boldsymbol{x}_{\text{poly}}$ can be estimated based on the least squares method

$$\boldsymbol{x}_{\text{poly}} = \left(\boldsymbol{B}_{\text{rss}}^T \boldsymbol{B}_{\text{rss}}\right)^{-1} \boldsymbol{B}_{\text{rss}}^T \boldsymbol{\varphi}_{\text{rss}} \tag{2}$$

In this case, the optimized ionospheric phase $\hat{\varphi}_{\mathrm{rss},0}$ at the target pixel (x_0, y_0) can be obtained by

$$\hat{\varphi}_{\mathrm{rss},0} = \begin{bmatrix} 1 & x_0 & y_0 \end{bmatrix} \cdot \boldsymbol{x}_{\mathrm{poly}} \tag{3}$$

Note that the PolyFit method is conducted on a pixel-by-pixel basis. In addition, the second-order polynomial, rather than the first-order polynomial used in Equation (1), can be used if spatial variation of the ionospheric delay is complicated. The ionospheric phases in the masked regions can be recovered by the surrounding valid signals. Furthermore, it is crucial to determine the maximum distance between the surrounding K pixels and the target pixel. Because the spatial variation of ionospheric delay cannot be previously determined, it is difficult to set a fixed threshold for maximum distance. Alternatively, it is recommended to determine the maximum distance by considering the real spatial pattern of the ionospheric delay. For example, given that the size of the whole region in Figure 3a is 3910×1132, the maximum distance is empirically set as 150 pixels. Figure 3f and Figure 3h show the ALOS2_DES_DInSAR observation before and after the ionospheric delay correction, respectively, in which the ionospheric phases have been significantly mitigated.

2.3 The SM-VCE method

In this study, the SM-VCE method (Liu et al., 2018) was used to calculate the 3-D displacements of the 2021 Maduo earthquake based on the above SAR displacement observations. Traditionally, the 3-D displacements at a target point are calculated from those displacement observations at this target point based on a weighted least squares (WLS) method (e.g., Fialko et al., 2005; Fialko et al., 2001; Jung et al., 2011; Wright et al., 2004), where the weights of these observations are determined based on the far-field observations that are assumed to be free of displacements or on the standard deviation of observations in a 5×5 pixel window around the target point (e.g., Hu et al., 2012; Jung et al., 2011). However, for a geophysical process (e.g., an earthquake), the ground surface displacements at adjacent points are generally related (with the exception of the fault-ruptured regions). The ignorance of this correlation is unrealistic and limits the accuracy of the 3-D displacements. In addition, the empirical weighting strategies cannot precisely reflect the accuracy of observations, and result in the reduced accuracy of the 3-D displacements. In the SM-VCE method (Liu et al., 2018), the strain model (SM) (Guglielmino et al., 2011) is employed to represent the correlation between adjacent points' displacements, and the weights of different observations are determined by the well-known variance component estimation (VCE) algorithm (Hu and Xiao 2016). In this case, the SM-VCE method is more accurate for obtaining 3-D displacements compared to the traditional WLS method (Hu et al., 2021; Liu et al., 2018; Liu et al., 2019). For completeness, Appendix B introduces the basic principles of the SM-VCE method, and the obtained 3-D displacements of the 2021 Maduo earthquake can be found in Section 3.1.

In the SM-VCE method, the number of adjacent points in the limited range is vital for the accuracy and efficiency of the method. In this case study, the window size was empirically determined to be 61×61 pixels because, at this spatial scale, the displacement-to-noise ratio of the POT-derived observations is sufficient for obtaining reliable 3-D displacements. Because obvious displacement jumps occurred across the fault region (see Figure 2), it is impracticable to use all of the available observations in the predefined window for the calculation of the 3-D displacements near the fault region. Based on the POT-derived observations (e.g., Figure 2) and Figure 2f), the fault traces can be manually mapped and then used to exclude the observations on the opposite side of the fault when calculating the 3-D displacements near the fault regions (Liu et al., 2021b).

Because the pixel resolution and coverage of the used SAR data are different, the 3-D displacements are calculated in the intersecting area of the footprints of descending ALOS-2 and ascending Sentinel-1 SAR data. Prior to the calculation of the 3-D displacements, all of the SAR displacement observations were resampled to the spatial grid of ascending Sentinel-1 displacement observations. Due to the contamination of serious ionospheric delay and decorrelations, the S1_DES_POT_AZI, ALOS2_AS_POT_AZI, ALOS2_AS_MAI, ALOS2_DES_POT_AZI, and ALOS2_DES_MAI observations (i.e., Figure 2g, 2k, 2l, 2o, and 2p)) were excluded, and only the remaining 11 observations in Figure 2 were used for the calculation of the 3-D displacements.

3. Results

3.1. Three-dimensional displacements of the 2021 Maduo earthquake

The 3-D displacements of the 2021 Maduo earthquake were obtained from the eleven ascending/descending Sentinel-1/ALOS-2 SAR displacements observations based on the SM-VCE method. As shown in Figure 4, it is easy to infer that the overall displacement pattern of this earthquake is consistent with the left-lateral strike-slip fault. The horizontal displacements are generally antisymmetric with respect to the fault ruptures of the 2021 Maduo earthquake, and the magnitude of the horizontal displacements in the northern part of the fault is larger than that in the southern part. The east–west (E-W) displacement component dominates the ground surface movements of the 2021 Maduo earthquake, with the maximum eastern and western displacements of 1.7 m and 2.4 m, respectively. Besides, it seems that the epicenter region exhibits the slighter E-W displacements along the fault trace, and the magnitude of E-W displacement becomes larger from the epicenter region to the eastern and to the western regions. This phenomenon is well consistent with the results of preliminary finite fault inversion. The finite slip model shows that those regions with large-magnitude horizontal displacements exist large amount of slip (Chen et al., 2021), indicating that the energy in these segments was possibly released to a considerable extent during the fault rupture process of the main shock. On the whole, the significant horizontal displacement field potentially indicates that the Tibetan Plateau is continuously affected by the tectonic stress field of the Indian plate pushing against the Eurasian plate, and the Bayankala block shows the characteristics of eastward movement (Wen 2018). The 2021 Maduo earthquake can be regarded as the result of the latest activity of the Bayankala block, which reflects the eastward escape movement of the Bayankala block (Xu et al., 2021). Compared with the horizontal displacement components, the vertical displacement component is more concentrated in the near-fault regions and the magnitude is smaller. Along the main fault rupture trace, an alternating uplift/subsidence phenomenon can be observed on both side of the fault, which suggests that the geometry of the seismogenic fault plane is not a simple vertical plane structure. The seismogenic fault can be divided into multiple segments with varying dip angles. Another thing to note is that the largest horizontal displacements of 2.4 m occurred around the northern side of the eastern fault region. Around this region, the horizontal displacements, particularly the north-south (N-S) displacements, appear to encounter a barrier that changes the displacement direction from southwest to northwest. It is speculated that displacements are blocked by two faults on the east side or by relatively tough materials on the southeast side (Xu et al., 2021).

The near-field global navigation satellite system (GNSS) horizontal coseismic displacements (see the circles in Figure 4) were used to assess the accuracy of the SAR-derived 3-D displacements. The root mean square errors (RMSEs) of the differences between the GNSS and the SAR-derived displacements are 5.2 and 12.2 cm in the E-W and N-S components, respectively. The RMSE value in the north component is relatively large. This might be biased by the GNSS station near the fault trace closest to the epicenter, where the difference in the N-S displacement between GNSS and SAR is up to 35 cm. This bias may be partly due to the very local ground fracture at this GNSS station caused by the strong seismic vibration. The low-precision SAR AZI displacements

could be another reason. We reevaluated the accuracy by excluding this site, resulting in the RMSE value of 6.4 cm for the north component. For comparison, the classical WLS method was also used to estimate the 3-D displacements of the 2021 Maduo earthquake. As shown in Figure S2, the WLS-derived 3-D displacements are significantly noisier compared to the SM-VCE result (Figure 4). The RMSEs between the GNSS and WLS-derived displacements are 9.3 and 37.0 cm in the E-W and N-S components, respectively, which indicates that improvements of 44% and 83% can be achieved in this case study by the SM-VCE method for the E-W and N-S components, respectively.

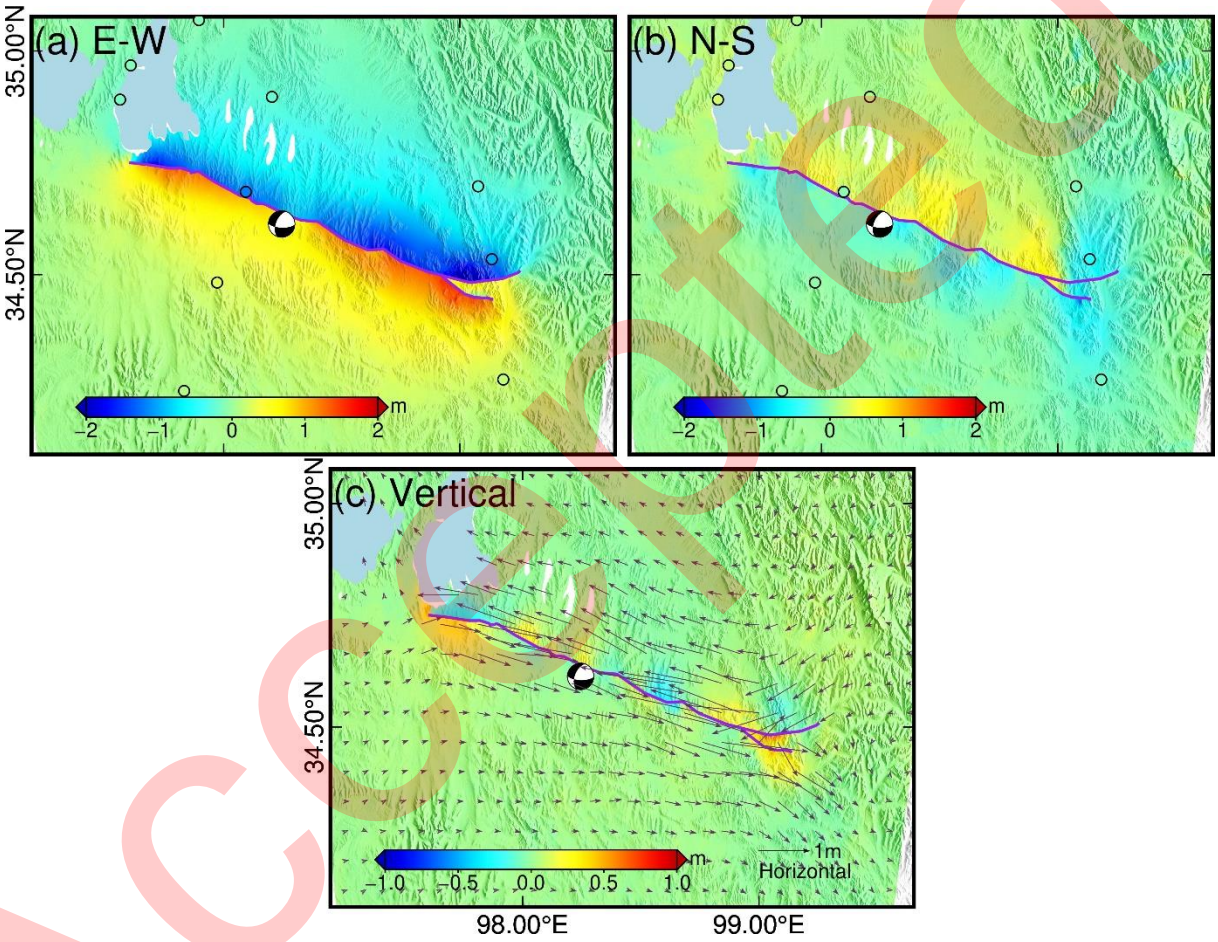

Figure 4. Three-dimensional coseismic displacements of the 2021 Maduo earthquake derived by the SM-VCE method. Circles in (a) and (b) show the locations of the GNSS stations, and their color indicates the GNSS-observed displacement. The arrows in (c) are the down-sampled horizontal displacements. The 3-D displacements within a greater range are shown in Figure S3.

3.2. Three strain invariants from the strain model

In addition to the ground surface displacements, the surface strain fields can also be used to interpret and describe the real geophysical behavior associated with seismic activities (Savage and Lisowski 1994). For the deformation analysis of a non-rigid body, three 2-D (i.e., the horizontal plane) strain invariants (i.e., dilatation, differential rotation, and maximum shear) with physical meaning are generally preferred (Goudarzi et al., 2015; Lin et al., 2010; Mehrabi 2021; Shen et al., 1996), and are independent of any shift and rotation of the coordinate systems. Detailed calculation of three strain invariants (i.e., dilatation, differential rotation, and maximum shear) can be found in Appendix C. Figure 5 presents the calculated strain invariants of the 2021 Maduo earthquake. For the dilatation map (Figure 5a), positive and negative values represent the regions experiencing extensional

and compressional deformations, respectively. The crosses represent the maximum and minimum normal strains, where the arrow orientation and the arrow length indicate the direction and magnitude of the strains, respectively. The extensional and compressional strains are shown as the inward and outward arrows, respectively. The eastern and western parts of the faults experience the most serious extensional and compressional deformations. This phenomenon is expected because the horizontal displacements change dramatically in these regions (see Figure 4). In addition, the region corresponding to extensional or compressional deformation is generally dominated by the extensional strain (the outward arrow) or the compressional strain (the inward arrow). In the differential rotation map (Figure 5b), the negative value indicates the clockwise rotation and the rotational wedges aim to better illustrate the magnitude and direction of the rotation. Both sides of the main faults experience the similar clockwise rotation, which is consistent with the horizontal displacement pattern in which the horizontal displacements gradually deviate to the right of their current displacement direction. The magnitude of rotation is large near the fault, and decreases with the distance from the fault. Similarly, due to the dramatic change in the horizontal displacements in the eastern and western parts of the faults, the rotation magnitude is very large in these regions. Regarding the maximum shear map (Figure 5c), the double-ended arrows represent the direction of the maximum shear, which is generally parallel to the orientation of the main fault. In addition, the shear signals are concentrated near the fault trace, and decrease with the distance from the fault. Since the region around the epicenter suffers smaller magnitude of deformations (see Figure 4a) compared with the eastern and western parts of the main fault, the magnitude of the rotation and shear around this region is also smaller than the eastern and western parts of the main fault.

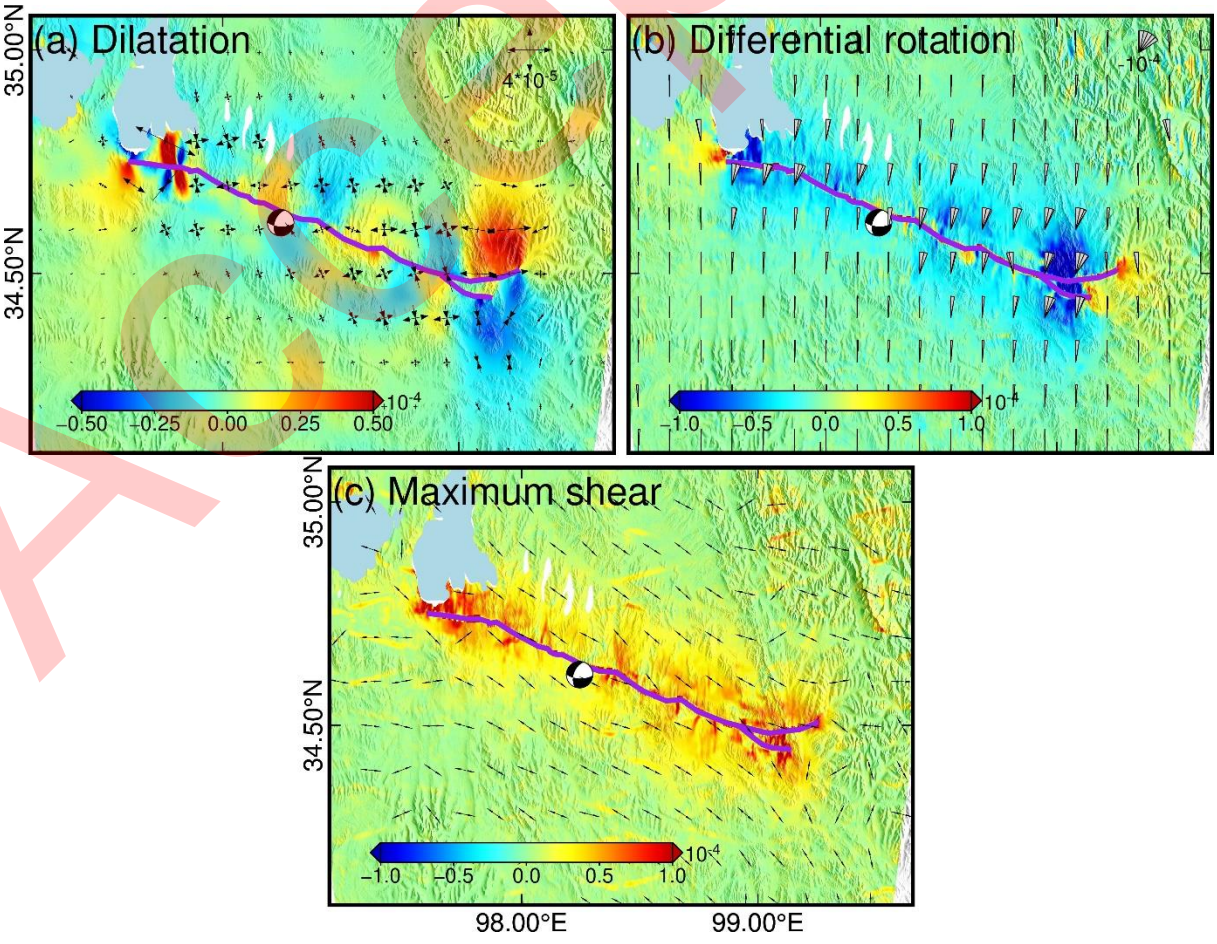

Figure 5. Three strain invariants for the 2021 Maduo earthquake. In (a), the crosses represent the maximum and minimum normal strains, where the arrow orientation and the arrow length are the direction and magnitude of

the strains, respectively. The extensional and compressional strains are shown as the outward and inward arrows, respectively. In (b), the rotational wedges are presented to better illuminate the magnitude and direction of the rotation. In (c), the direction of the double-sided arrow represents the direction of the maximum shear. The strain fields within a greater range are shown in Figure S4.

4. Discussions

4.1 The importance of BOI observations for the N-S displacement component

Since the BOI method can only obtain AZI displacements in the burst overlap area, this method is not commonly used for displacement monitoring like the DInSAR, MAI, and POT methods. However, some cases have demonstrated that this method can provide important AZI displacement information (e.g., Grandin et al., 2016; He et al., 2018; Jiang et al., 2017), particularly for earthquakes. Among the SAR displacement observations for the 2021 Maduo earthquake in this paper, with the exception of the BOI observations, the N-S displacement component can only be well constrained by the S1_POT_AZI observations. However, the accuracy of the S1_POT_AZI observations is too low to obtain high-precision N-S displacements. Therefore, it is expected that the BOI observations with higher accuracy compared to the S1_POT_AZI are of great significance in the calculation of the N-S displacement.

To highlight the importance of BOI observations for the N-S displacement component, the 3-D displacements were calculated by the SM-VCE method without the BOI observations. As shown in Figure S5, it was found that the spatial pattern is very similar between the 3-D displacements in Figure S5 (without the BOI observations) and in Figure 4 (with the BOI observations). However, the N-S displacement component is noisier when the BOI observations are not used. Compared with the GNSS data, the RMSE values are 5.4 and 13.7 cm for the E-W and N-S displacement components, respectively, indicating that significant improvement of about 53% can be achieved for the N-S component in this study when the BOI observations are combined.

At present, most applications of the BOI method are for large magnitudes of displacements (e.g., earthquakes) with only one pair of SAR images. By combining the SAR time-series data, some researchers have attempted to obtain millimeter-level AZI displacements with respect to the plate inter-seismic movement (e.g., Li et al., 2021a). This achievement is exciting because such a small magnitude of displacement can only be captured by the multi-temporal InSAR (MT-InSAR) method, which is only sensitive to the E-W and vertical components. The AZI displacement observations obtained by the BOI method can well complement the DInSAR-derived observations, and then can be used to realize a time series of 3-D displacement monitoring. The BOI method benefits from the open data policy and the regular acquisition of Sentinel-1 data, and thus can gradually become a routine tool for displacement monitoring, therefore providing important displacement observations for various geohazards.

4.2 The implication of three strain invariants in coseismic events

Strain describes the non-rigid body deformation, which is a geometric concept used to quantify the relative displacement and subsequent changes in particle configuration in each dimension of the body (Cardozo and Allmendinger 2009). The dilatation invariant corresponds to the volume compression and extension of the Earth body. For example, given that two forces are added in both sides of a block, if the direction of these two forces is toward the center, the volume of this block would be compressed and the dilatation value at this point is negative; if the direction of these two forces is away from the center, the volume of this block would be extended and the dilatation value at this point is positive. The differential rotation represents the rotating trend of the horizontal displacements. If the horizontal displacements are towards the same direction within a region, the rotation value

is zero. However, when the horizontal displacements gradually deviate from their current displacement direction, the rotation value represents the direction and magnitude of the rotation. Finally, maximum shear is generated in the region where relative displacements occur. For example, if the directions of the horizontal displacements of the adjacent two points are similar, but the magnitude is different, maximum shear strain occurs along the displacement direction.

Most of the existing researches focus on the study related to the interseismic strain fields. Similar to the interseismic strain fields, the coseismic strain fields are also estimated based on the displacement gradients. The main difference is that the interseismic strain fields are generally derived from the on-going long-term small-magnitude deformations, whereas the coseismic strain fields are obtained based on the transient deformations that have occurred. In this case, the interseismic strain fields can be used to assess the future risk of the fault, and the coseismic strain fields can be used for the disaster assessment. For example, large magnitudes of the strain fields mean that the corresponding area may have been severely deformed, and the ground surface and man-made structures (such as bridges and roads) may have been severely damaged. If future seismic activity occurs in the nearby area, the surface with large magnitude of strain invariants may be more vulnerable than elsewhere. Besides, the coseismic strain fields can also be used to identify the regions with unobvious surface ruptures (Hu et al., 2020; Xu et al., 2020), where the coseismic strain fields usually show higher magnitudes compared to the rupture-free regions.

5. Conclusions

The 2021 Maduo earthquake, Qinghai Province, China, was the largest earthquake in China since the 2008 Wenchuan earthquake. In this study, we derived the complete 3-D coseismic displacements associated with this earthquake using both C-band Sentinel-1 and L-band ALOS-2 SAR data from ascending/descending tracks. Up to eleven high-quality SAR displacement observations in the geometries of ascending/descending LOS/AZI directions were obtained based on the DInSAR, POT, BOI, and MAI methods. Because the RSS-derived ionospheric phases are highly sensitive to the decorrelation noise, a polynomial fitting method was proposed to correct the ionospheric phase delay in the L-band ALOS-2 DInSAR interferograms. The accurate 3-D displacement field of the 2021 Maduo earthquake was obtained using the SM-VCE method to intuitively reveal the real ground surface movement. It was found that this earthquake was dominated by a left-lateral fault slip with the largest horizontal displacement of up to 2.4 m. The vertical displacement component is more concentrated in the near-fault regions and with a smaller magnitude, and an alternating uplift/subsidence phenomenon can be observed on both side of the main fault. Comparison with the GNSS data indicates that the SM-VCE method can significantly improve the horizontal displacements compared to the classical WLS method, and the incorporation of the BOI displacements can substantially increase the accuracy of the N-S displacement component. In addition to the surface displacement, the strain field is another physical quantity that can be used to quantify the relative displacement within the Earth body. Based on the strain model parameters estimated by the SM-VCE method, three strain invariants (i.e., dilatation, differential rotation, and maximum shear) were calculated and analyzed. The results showed that the eastern and western parts of the faults suffered significant strains, but the epicenter region was less affected by the rotation and shear strains. The displacement result and the fault slip model used in this study can be freely accessed, which will be useful for the broad community that is studying this earthquake.

Acknowledgments

The ALOS-2 data were provided by the Japan Aerospace Exploration Agency (JAXA) (https://auig2.jaxa.jp/ips/home, PI No. PER2A2N038), and the Sentinel-1 data were provided by ESA/Copernicus

(https://scihub.copernicus.eu/). We thank the associate editor and two anonymous reviewers for their constructive comments and suggestions. This work was supported by the National Key Basic Research and Development Program of China (No. 2018YFC1503603), the National Natural Science Foundation of China (No. 42030112), the Nature Science Foundation of Hunan Province (No. 2020JJ2043), the Project of Innovation-driven Plan of Central South University (No. 2019CX007), by the Fundamental Research Funds for the Central Universities of Central South University (Nos. 2018zzts684 and 2019zzts011), and by the Hunan Provincial Innovation Foundation For Postgraduate (No. CX20190067). The displacement result and the fault slip model in this paper can be freely accessed through https://dx.doi.org/10.5281/zenodo.5009820.

References

Bechor N B D, Zebker H A. 2006. Measuring two-dimensional movements using a single InSAR pair. Geophys Res Lett, 33: 275-303

Bürgmann R, Schmidt D, Nadeau R M, D'Alessio M, Fielding E, Manaker D, McEvilly T V, Murray M H. 2000. Earthquake potential along the Northern Hayward fault, California. Science, 289: 1178-1182

Cardozo N, Allmendinger R W. 2009. SSPX: A program to compute strain from displacement/velocity data. Comput Geosci, 35: 1343-1357

Chen H, Qu C, Zhao D, Ma C, Shan X. 2021. Rupture Kinematics and Coseismic Slip Model of the 2021 Mw 7.3 Maduo (China) Earthquake: Implications for the Seismic Hazard of the Kunlun Fault. Remote Sensing, 13: 3327

Clarke P J, Davies R R, England P C, Parsons B, Billiris H, Paradissis D, Veis G, Cross P A, Denys P H, Ashkenazi V, Bingley R, Kahle H G, Muller M V, Briole P. 1998. Crustal strain in central Greece from repeated GPS measurements in the interval 1989-1997. Geophys J Int, 135: 195-214

Fialko Y. 2004. Evidence of fluid-filled upper crust from observations of postseismic deformation due to the 1992 Mw7. 3 Landers earthquake. J Geophys Res Solid Earth, 109, http://doi.org/10.1029/2004JB002985

Fialko Y, Sandwell D, Simons M, Rosen P. 2005. Three-dimensional deformation caused by the Bam, Iran, earthquake and the origin of shallow slip deficit. Nature, 435: 295-299

Fialko Y, Simons M, Agnew D. 2001. The complete (3-D) surface displacement field in the epicentral area of the 1999 M W 7.1 Hector Mine Earthquake, California, from space geodetic observations. Geophys Res Lett, 28: 3063–3066

Funning G J, Garcia A. 2019. A systematic study of earthquake detectability using Sentinel-1 InterferometricWide-Swath data. Geophys J Int, 216: 332-349

Funning G J, Parsons B, Wright T J, Jackson J A, Fielding E J. 2005. Surface displacements and source parameters of the 2003 Bam (Iran) earthquake from Envisat advanced synthetic aperture radar imagery. J Geophys Res Solid Earth, 110, http://doi.org/10.1029/2004JB003338

Gabriel A K, Goldstein R M, Zebker H A. 1989. Mapping small elevation changes over large areas: Differential radar interferometry. J Geophys Res Solid Earth, 94: 9183-9191

Gan J, Hu J, Li Z, Yang C, Liu J, Sun Q, Zheng W. 2018. Mapping three-dimensional co-seismic surface

deformations associated with the 2015 Mw7.2 Murghab earthquake based on InSAR and characteristics of crustal strain. Sci China Earth Sci, 61: 1451-1466

Goudarzi M A, Cocard M, Santerre R. 2015. GeoStrain: An open source software for calculating crustal strain rates. Comput Geosci, 82: 1-12

Grandin R, Klein E, Métois M, Vigny C. 2016. 3D displacement field of the 2015 M w 8.3 Illapel earthquake (Chile) from across- and along-track Sentinel-1 TOPS interferometry. Geophys Res Lett, 43: 2552-2561

Guglielmino F, Nunnari G, Puglisi G, Spata A. 2011. Simultaneous and Integrated Strain Tensor Estimation From Geodetic and Satellite Deformation Measurements to Obtain Three-Dimensional Displacement Maps. IEEE Trans Geosci Remote Sens, 49: 1815-1826

He P, Wen Y, Xu C, Chen Y. 2018. High-quality three-dimensional displacement fields from new-generation SAR imagery: application to the 2017 Ezgeleh, Iran, earthquake. J Geod, 93: 573-591

He P, Wen Y, Xu C, Chen Y. 2019. Complete three-dimensional near-field surface displacements from imaging geodesy techniques applied to the 2016 Kumamoto earthquake. Remote Sens Environ, 232: 111321

Hu J, Li Z, Zhu J, Zhang L, Sun Q. 2012. 3D coseismic Displacement of 2010 Darfield, New Zealand earthquake estimated from multi-aperture InSAR and D-InSAR measurements. J Geod, 86: 1029-1041

Hu J, Liu J, Li Z, Zhu J, Wu L, Sun Q, Wu W. 2021. Estimating three-dimensional coseismic deformations with the SM-VCE method based on heterogeneous SAR observations: Selection of homogeneous points and analysis of observation combinations. Remote Sens Environ, 255: 112298

Hu J, Wang Q J, Li Z W, Xie R A, Zhang X Q, Sun Q. 2014. Retrieving three-dimensional coseismic displacements of the 2008 Gaize, Tibet earthquake from multi-path interferometric phase analysis. Nat Hazards, 73: 1311-1322

Hu S W, Xiao B L. 2016. Modern theory and application of surveying data processing (in Chinese). Beijing, China: Surveying and Mapping Press.

Hu X, Bürgmann R, Schulz W H, Fielding E J. 2020. Four-dimensional surface motions of the Slumgullion landslide and quantification of hydrometeorological forcing. Nat Commun, 11: 2792

Intrieri E, Raspini F, Fumagalli A, Lu P, Conte S D, Farina P, Allievi J, Ferretti A, Casagli N. 2018. The Maoxian landslide as seen from space: detecting precursors of failure with Sentinel-1 data. Landslides, 15: 123-133

Jacobs A, Sandwell D, Fialko Y, Sichoix L. 2002. The 1999 (M w 7.1) Hector Mine, California, earthquake: Near-field postseismic deformation from ERS interferometry. Bull Seismol Soc Am, 92: 1433-1442

Jiang H, Feng G, Wang T, Bürgmann R. 2017. Toward full exploitation of coherent and incoherent information in Sentinel-1 TOPS data for retrieving surface displacement: Application to the 2016 Kumamoto (Japan) earthquake. Geophys Res Lett, 44: 1758–1767

Jung H S, Lu Z, Won J S, Poland M P, Miklius A. 2011. Mapping Three-Dimensional Surface Deformation by Combining Multiple-Aperture Interferometry and Conventional Interferometry: Application to the June 2007 Eruption of Kilauea Volcano, Hawaii. IEEE Geosci Remote Sens Lett, 8: 34-38

Jung H S, Won J S, Kim S W. 2009. An Improvement of the Performance of Multiple-Aperture SAR Interferometry (MAI). IEEE Trans Geosci Remote Sens, 47: 2859-2869

Li X, Jónsson S, Cao Y. 2021a. Interseismic deformation from Sentinel-1 burst-overlap interferometry: Application to the southern Dead Sea fault. Geophys Res Lett, 48: e2021GL093481

Li Y, Bürgmann R. 2021. Partial coupling and earthquake potential along the Xianshuihe Fault, China. J Geophys Res Solid Earth, 126: e2020JB021406

Li Y, Huang L, Ding R, Yang S, Liu L, Zhang S, Liu H. 2021b. Coulomb stress changes associated with the M7.3 Maduo earthquake and implications for seismic hazards. Nat Hazard Res, http://doi.org/10.1016/j.nhres.2021.06.003

Li Z, Ding K, Zheng P, Wen Y, Zhao L, Chen J. 2021c. Co-seismic Deformation and Slip Distribution Of 2021 Mw 7.4 Madoi Earthquake from GNSS Observation. Geomatics and Information Science of Wuhan University: 1-10, http://doi.org/10.13203/j.whugis20210301

Lin K C, Hu J C, Ching K E, Angelier J, Rau R J, Yu S B, Tsai C H, Shin T C, Huang M H. 2010. GPS crustal deformation, strain rate and seismic activity after the 1999 Chi-Chi earthquake in Taiwan. J Geophys Res Solid Earth, 115: 1-22

Liu J, Hu J, Burgmann R, Li Z, Sun Q, Ma Z. 2021a. A Strain-Model Based InSAR Time Series Method and its Application to The Geysers Geothermal Field, California. J Geophys Res Solid Earth, 126: e2021JB021939

Liu J, Hu J, Li Z, Zhu J. 2021b. Estimation of 3D coseismic deformation with InSAR: an improved SM-VCE method by window optimization. Acta Geodaetica Et Cartographica Sinica, 50: 1-18

Liu J, Hu J, Li Z, Zhu J J, Sun Q, Gan J. 2018. A Method for Measuring 3-D Surface Deformations With InSAR Based on Strain Model and Variance Component Estimation. IEEE Trans Geosci Remote Sens, 56: 239-250

Liu J, Hu J, Xu W, Li Z, Zhu J, Ding X, Zhang L. 2019. Complete three-dimensional co-seismic deformation fields of the 2016 Central Tottori earthquake by integrating left- and right-looking InSAR with the improved SM-VCE method. J Geophys Res Solid Earth, 124: 12099–12115

Ma Z, Jiang M, Khoshmanesh M, Cheng X. 2021. Time Series Phase Unwrapping Based on Graph Theory and Compressed Sensing. IEEE Trans Geosci Remote Sens: 1-19, http://doi.org/10.1109/TGRS.2021.3066784

Mehrabi H. 2021. Three-dimensional strain descriptors at the Earth's surface through 3D retrieved co-event displacement fields of differential interferometric synthetic aperture radar. J Geod, 95: 1-16

Michel R, Avouac J P, Taboury J. 1999. Measuring ground displacements from SAR amplitude images: Application to the Landers Earthquake. Geophys Res Lett, 26: 875-878

Okada Y. 1985. Surface deformation to shear and tensile faults in a halfspace. Bull Seismol Soc Am, 75: 1018-1040

Pan J, Bai M, Li C, Liu F, Li H, Liu D, Chevalier M-L, Wu K, Wang P, Lu H, Chen P, Li C. 2021. Coseismic surface rupture and seismogenic structure of the 2021-05-22 Maduo (Qinghai) Ms7.4 earthquake. Acta Geol Sin, 95: 1655-1670

Pietrantonio G, Riguzzi F. 2004. Three-dimensional strain tensor estimation by GPS observations: methodological aspects and geophysical applications. J Geodyn, 38: 1-18

Savage J C, Lisowski M. 1994. Strain accumulation north of Los Angeles, California, as a function of time, 1977–1992. Geophys Res Lett, 21: 1173-1176

Shen Z-K, Jackson D D, Ge B X. 1996. Crustal deformation across and beyond the Los Angeles basin from geodetic measurements. J Geophys Res Solid Earth, 101: 27957-27980

Shi X, Wang Y, Jing L Z, Weldon R, Wei S, Wang T, Sieh K. 2017. How complex is the 2016 Mw 7.8 Kaikoura earthquake, South Island, New Zealand? *Sci Bull*, 62: 309-311

Teza G, Pesci A, Galgaro A. 2008. Grid_strain and grid_strain3: Software packages for strain field computation in 2D and 3D environments. Comput Geosci, 34: 1142-1153

Torres R, Snoeij P, Geudtner D, Bibby D, Davidson M, Attema E, Potin P, Rommen B, Floury N, Brown M. 2012. GMES Sentinel-1 mission. Remote Sens Environ, 120: 9-24

Wang T, Wei S, Shi X, Qiu Q, Li L, Peng D, Weldon R J, Barbot S. 2018. The 2016 Kaikōura earthquake: Simultaneous rupture of the subduction interface and overlying faults. Earth Planet Sci Lett, 482: 44-51

Wang W, Fang L, Wu J, Tu H, Chen L, Lai G, Zhang L. 2021. Aftershock sequence relocation of the 2021 Ms7.4 Maduo Earthquake, Qinghai, China. Sci China Earth Sci, 64(8): 1371-1380

Wen X-Z. 2018. The 2008 Wenchuan, 2013 Lushan and 2017 Jiuzhaigou earthquakes, Sichuan, in the last more than one thousand years of rupture history of the eastern margin of the Bayan Har block. Acta Seismol Sin, 40: 255-267

Wright T J, Parsons B E, Lu Z. 2004. Toward mapping surface deformation in three dimensions using InSAR. Geophys Res Lett, 31: 169-178

Xu W, Feng G, Meng L, Zhang A, Ampuero J P, Bürgmann R, Fang L. 2018. Transpressional Rupture Cascade of the 2016 Mw 7.8 Kaikoura Earthquake, New Zealand. J Geophys Res Solid Earth, 123: 2396–2409

Xu X, Sandwell D T, Ward L A, Milliner C W D, Smith-Konter B R, Fang P, Bock Y. 2020. Surface deformation associated with fractures near the 2019 Ridgecrest earthquake sequence. Science, 370: 605-608

Xu Z, Liang S, Zhang G, Liang J, Zou L, Li X, Chen Y. 2021. Analysis of seismogenic structure of Madoi, Qinghai M S 7.4 earthquake on May 22, 2021. Chin J Geophys: 2657-2670

Zhan Y, Liang M, Sun X, Huang F, Zhao L, Gong Y, Han J, Li C, Zhang P, Zhang H. 2021. Deep structure and seismogenic pattern of the 2021.5.22 Madoi (Qinghai) MS7.4 earthquake. J Geophys, 64: 2232-2252

Zhu Y, Diao F, Fu Y, Liu C, Xiong X. 2021. Slip rate of the seismogenic fault of the 2021 Maduo earthquake inferred from GPS observations. Sci China Earth Sci, 64(8): 1363-1370